Chemical Engineering Journal 416 (2021) 129112

Contents lists available at ScienceDirect

Chemical Engineering Journal

journal homepage: www.elsevier.com/locate/cej

In-situ synthesis of Z-Scheme MIL-100(Fe)/α-Fe_2O_3 heterojunction for enhanced adsorption and Visible-light photocatalytic oxidation of O-xylene

Lu Chen [a,b], Xiao Wang [a,*], Zepeng Rao [a], Zixia Tang [a], Yan Wang [a], Gansheng Shi [a], Guanhong Lu [a], Xiaofeng Xie [a], Deliang Chen [b,c], Jing Sun [a]

[a] State Key Lab of High Performance Ceramics and Superfine Microstructure, Shanghai Institute of Ceramics, Chinese Academy of Sciences, 585 Heshuo Road, Shanghai 201899, China
[b] School of Materials Science and Engineering, Zhengzhou University, Zhengzhou 450001, China
[c] School of Materials Science and Engineering, Dongguan University of Technology, Dongguan 523808, China

ARTICLE INFO

Keywords:
In-situ synthesis
Z-Scheme
MIL-100(Fe)/α-Fe_2O_3
Photocatalytic oxidation
VOCs

ABSTRACT

Though exhibiting excellent performance in the adsorption of organic gas pollutants, the application of MOFs is still limited in the photocatalytic oxidation (PCO) of volatile organic compounds (VOCs) due to the short lifetime of photogenerated electron-hole pairs. MIL-100(Fe)/α-Fe_2O_3 photocatalysts were fabricated through a facile one-step hydrothermal method by adjusting the coordination of Fe(III) ions for the PCO of typical VOCs. The large specific surface area (763 $m^2 g^{-1}$), uniformly distributed active sites and suitable pore structure of the composites enable the effective adsorption of target o-xylene molecules. The MIL-100(Fe)/α-Fe_2O_3 hybrid presented a high o-xylene removal efficiency of 100% under 250 W xenon (Xe) lamp irradiation and 90% under visible light ($\lambda \geq$ 420 nm), which is far beyond the performance of commercial TiO_2 photocatalyst under the same conditions (23% under 250 W Xe lamp irradiation and 0% under visible light). The ESR results confirmed the formation of Z-scheme structure and revealed that the reversible conversion of Fe(III) and Fe(II) under light irradiation plays a key role in the oxidation of o-xylene and the effective generation of reactive radicals. The PCO mechanism of o-xylene was analyzed through in-situ DRIFTS. This work not only provides a means for the synthesis and optimization of high performance photocatalysts based on MOFs for air purification, but also shed light on the PCO mechanism of o-xylene by MOFs photocatalysts.

1. Introduction

Volatile organic compounds (VOCs) have caused adverse effects on the ecological environment and human health due to its toxicity and environmental persistence. Aromatics is the most important VOC group in several megacities, accounting for 20 ~ 50% of the measured VOC reactivity, which is mainly caused by vehicle emissions and industries [1,2]. Therefore, the elimination of aromatics, is of great significance to the purification of atmospheric environment. Photocatalytic oxidation (PCO) has been proven to be promising means in the mineralization of VOCs [3]. Since the work by Fujishima and Honda in 1972, TiO_2-based photocatalysts have drawn tremendous attention in the PCO of VOCs due to their high stability, low cost and easy accessibility [4]. Efforts have been performed to optimize the activity of TiO_2-based photocatalysts for the rapid and complete mineralization of typical VOCs [5,6]. Despite all these efforts, TiO_2-based photocatalysts still suffer from several drawbacks, such as the poor affinity to aromatic hydrocarbons, the fast recombination of electron-hole pairs, limited PCO activity under visible light and easily be deactivated [7]. These shortcomings severely limit the application of photocatalytic technology in the degradation of aromatic pollutants. The effective elimination of VOCs by photocatalyst oxidation calls for the development of alternatives with good capture ability for aromatic hydrocarbons and high PCO activity.

Most metal–organic frameworks (MOFs) are semiconductor-like porous materials composed of metal-oxo clusters and organic coordinated ligands [8]. In addition to their tremendous specific surface areas (SSA) and spatially arranged active sites, which enable their application in the capture of gaseous molecules such as CO_2, O_3 and VOCs, MOFs also exhibit excellent ligand–metal charge transfer (LMCT) property as promising candidates for the PCO of organic pollutants [9–11]. In fact, some MOFs such as the ones based on Titanium [12], Zirconium [13]

* Corresponding author.
E-mail address: wangxiao@mail.sic.ac.cn (X. Wang).

https://doi.org/10.1016/j.cej.2021.129112
Received 17 December 2020; Received in revised form 8 February 2021; Accepted 19 February 2021
Available online 25 February 2021

and iron [14,15] have already been proven to be high-performance photocatalysts for the degradation of dyes and the splitting of water. Among various MOFs, ion-based MOFs such as MIL-100(Fe), MIL-101 (Fe) and MIL-88(Fe) have drawn lots of interests not only because of their high abundance and low toxicity, but also for their suitable HOMO-LUMO gap of around 2 eV and LMCT property under visible light. The high specific surface area, suitable pore size, uniformly distributed Fe active sites and aromatic ligand structure are conducive to the rapid adsorption and decomposition of VOCs, especially aromatic hydrocarbons. Li et al. [16] confirmed that Fe-MOFs could work as promising candidates for the PCO of toluene. However, the relatively lower HOMO state of Fe-MOFs (1.73 eV for MIL-100(Fe) and 0.98 eV for MIL-101(Fe)) was not sufficient for the generation of active •OH radicals through the oxidation of H_2O (2.34 eV) [17–19]. As •OH radical is one of the main radicals required for the PCO of VOCs, the lack of •OH radical may severely limit the performance of Fe-MOFs as a photocatalyst. Secondly, Fe-MOFs suffers from the fast recombination of photon-induced electron-hole pairs due to its small HOMO-LUMO gap, which impedes the fully utilization of the light energy.

Building a two-step photoexcitation system (Z-scheme) has been proven to be a promising method for improving the utilization of photons without sacrificing the high SSA and visible-light activity of MOFs. Herein, MIL-100(Fe)/α-Fe_2O_3 composites with an artificial Z-scheme structure were synthesized through a facile one-step hydrothermal method. A typical aromatic pollutant, o-xylene, was chosen as the target pollutant to evaluate the performance of the composites. The high SSA and π-π interaction between MIL-100(Fe) and o-xylene enabled the fast and effective capture of target molecules. The direct and close contact between the two components enabled the fast charge transfer at the interfaces and the effective separation of electron-hole pairs. Compared with pristine α-Fe_2O_3 or MIL-100(Fe), MIL-100(Fe)/α-Fe_2O_3 exhibit an improved performance in the PCO of o-xylene under the irradiation of both Xe lamp and visible light. Further mechanism study through ESR and in-situ DRIFTS analysis reveals that the outstanding performance of MIL-100(Fe)/α-Fe_2O_3 not only originates from the high SSA and uniform distribution of active sites, promoting the adsorption of o-xylene, but also benefits from the direct transfer of charge carriers between the active sites and o-xylene molecules, as well as the effective generation of both •O_2^- and •OH radicals. The construction of in-situ Z-scheme structure based on Fe-MOFs and results reported here would provide a new sight for the application of MOFs in the PCO of gaseous organic pollutants.

2. Experimental section

2.1. Materials

Commercially available chemicals were used without additional purification. 1,3,5-benzenetricarboxylic acid (H_3BTC), Iron nitrate nonahydrate ($Fe(NO_3)_3{\cdot}9H_2O$) and ethanol were purchased from Sinopharm Chemical Reagent Co., Ltd, and Shanghai Zhenxing chemical No.1 plant, respectively. Deionized water (18.2MΩ) was used during analysis.

2.2. Sample preparation

2.2.1. Preparation of the MIL-100(Fe)/α-Fe_2O_3

The sample MIL-100(Fe)/α-Fe_2O_3 was synthesized by a modified hydrothermal method [20]. In a typical procedure, 6 mmol Fe $(NO_3)_3{\cdot}9H_2O$ was dissolved into 60 mL deionized water and then 6 mmol H_3BTC was added to the above solution at the stirring speed of 650 r/min for a certain time (15 and 30 min, respectively). The obtained orange solution was then transferred to a 100 mL Teflon-lined autoclave and kept at 150 °C for 12 h. After cooling down to room temperature, the product was collected by centrifugation and washed with deionized water and ethanol for three times. The solid powders of MIL-100(Fe)/α-Fe_2O_3 were finally obtained after drying in a vacuum oven at 60 °C for 16 h. The hybrids are termed hereafter MIL-100(Fe)/α-Fe_2O_3-15 and 30, where the numbers indicate the stir time (unit: min) in the previous step (Scheme S(1)).

2.2.2. Preparation of the MIL-100(Fe) and α-Fe_2O_3

MIL-100(Fe) was obtained by the above fabrication method of MIL-100(Fe)/α-Fe_2O_3 hybrid materials. Maintaining the same stirring speed, the Fe(III) and the organic ligand H_3BTC in the solution were completely coordinated through extending the stirring time to an hour to obtain MIL-100(Fe) without α-Fe_2O_3. The synthesis method and steps of α-Fe_2O_3 were the same as the preparation of MIL-100(Fe)/α-Fe_2O_3 materials, except that H_3BTC was not added during the synthesis process.

2.3. Characterization

The X-ray diffraction (XRD) measurement of the samples was carried out on EMYPREAN diffractometer with monochromatized Cu Kα radiation (k = 1.5418 Å) over a 2theta degree of 5°-80°. The Fourier Transform Infrared spectroscopy (FTIR, Vertex 70, ThermoFisher Scientific) was carried out to research the structure information of the materials in the range of 4000–500 cm^{-1}. The Brunauer-Emmett-Teller (BET) surface area, nitrogen adsorption–desorption isotherm, and porosity distribution were studied through Micromeritics ASAP 3000 at 77 K. The X-ray photoelectron spectroscopy (XPS) measurement was used to analyze the elemental valence state and the surface chemical environment by the ESCAlab250 (USA) instrument. The UV–vis absorption spectra of the as-prepared samples were recorded through the UV–vis diffuse reflectance spectroscopy (DRS) (Cary 5000, USA) and barium sulfate was used as a standard of reflectance. Photoluminescence (PL) spectroscopy was conducted on an LS55 spectrometer of Perkin Elmer Instruments with the wavelength of 320 nm. Thermogravimetric analysis (TGA) was carried out on a thermo analyzer (STA449C, NETZSCH) with a heating rate of 10 °C/min from room temperature to 700 °C under air. *In situ* Diffuse Reflection Infrared Fourier Transform spectroscopy (DRIFTS) was carried out on the Shimadzu IRTracer-100 instrument, equipped with a mercury cadmium telluride (MCT) detector cooled by liquid nitrogen to research the degradation pathway of o-xylene. The transient photocurrent test was achieved on photoelectrochemical workplace (CHI 650B, CH instruments Inc., Shanghai) with a three-electrodes-system and an electrolyte solution of NaCl (0.5 mol/L). The Ag/AgCl and Pt foil served as the reference and counter electrodes, respectively. The samples were coated on FTO disks by spin coating to act as the work electrode.

2.4. ESR test

Electron spin resonance (ESR) signal of active radicals trapped by 5,5-dimethyl-1-pyrroline N-oxide (DMPO) was recorded on a JES-FA200 spectrometer. DMPO was purchased from DOJINDO Laboratories with purity higher than 99% as claimed by the producer. Samples for ESR measurements were prepared by mixing 4 mg sample with 5 mL liquid (deionized water for DMPO-•OH and ethanol for DMPO-•O_2^- ultrasonically dispersed for 5 min, respectively). 6 μL DMPO was added into 200 μL of the mixed solution under a Xe lamp irradiation.

2.5. Adsorption and photocatalytic activity

The adsorption and photocatalytic degradation activity towards o-xylene of the samples were tested in a flow phase reaction system at ambient temperature as reported previously shown in Scheme S(2) [21]. The reaction chamber with a volume of 120 mL (15 × 8 × 1 cm) was covered by a quartz glass plate. The 250 W xenon lamp was placed 30 cm above the sample as the light irradiation source. Firstly, the photocatalyst (0.095 g) loaded on a glass slide (12 × 5 cm) was placed in the chamber, and then 50 ppm o-xylene flowed through the cuboid quartz

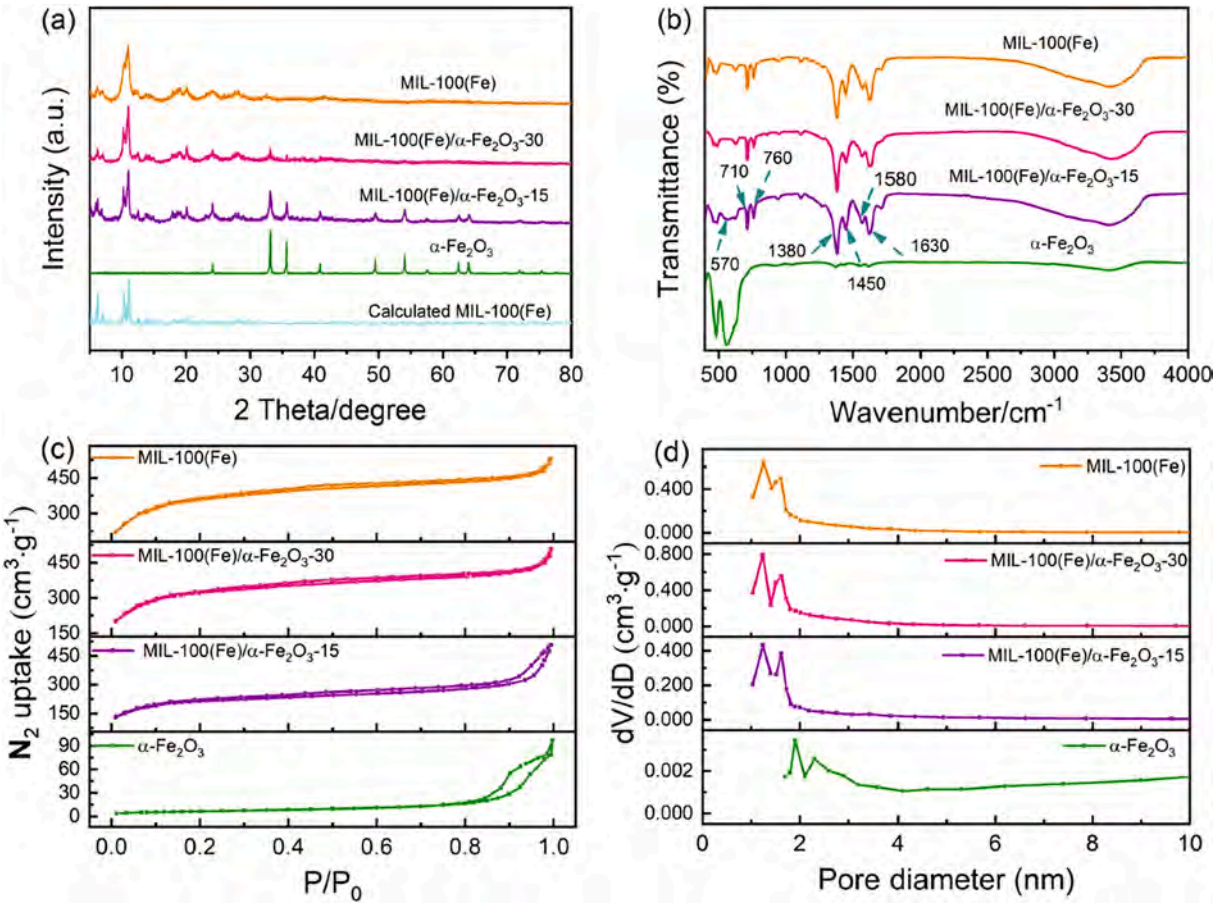

Fig. 1. Characterization of the as-prepared samples (a) XRD (b) FTIR spectra (c) BET (d) Pore size distributions from nitrogen adsorption isotherms.

vessel at a flow rate of 10 mL/min. Meanwhile the air passed through the humidification tank at a flow rate of 10 mL/min and mixed with o-xylene flow in gas-mixed jar, and then entered into the cuboid quartz vessel. A blank experiment with no photocatalyst loading on the glass slide was also carried out to confirm the role of photocatalysts. The concentration of o-xylene is 25 ppm. It took approximately 220 min to reach an adsorption–desorption equilibrium in the dark. After the adsorption–desorption equilibrium was reached, the photocatalytic activity experiment was performed under the 250 W Xe lamp or visible light with a 420 nm filter. The concentration of o-xylene was measured by a gas chromatography (GC-7920, Beijing China Education Au-light Co., Ltd., China) with a flame ionization detector (FID) detector. The removal ratio (η) of o-xylene was calculated according to the following formula, where C_0 and C were the initial and the real-time concentration of o-xylene, respectively.

$$\eta = (1 - C/C_0) \times 100\%$$

3. Results and discussion

3.1. Characterization of morphology, structure, composition and optical properties

The composition and crystal structure of α-Fe_2O_3, MIL-100(Fe)/α-Fe_2O_3-15, MIL-100(Fe)/α-Fe_2O_3-30 and MIL-100(Fe) were analyzed by XRD. As shown in Fig. 1(a), diffraction peaks of the as-prepared α-Fe_2O_3 sample were well matched with the standard card of α-Fe_2O_3 (JCPDS No. 33–0664) [22]. The positions of all peaks of the MIL-100(Fe) sample were in good agreement with the XRD standard spectrum of MIL-100(Fe) obtained by Horcajada et al. through Rietveld refinement, confirming the successfully synthesis of MIL-100(Fe) [23,24]. The peak positions of the composites matched well with the diffraction pattern of MIL-100(Fe) in the range of 5 to 30° and the diffraction peaks at 33.1° and 35.6°could be assigned to the (1 0 2) and (1 1 0) facets of α-Fe_2O_3, which indicated the formation of MIL-100(Fe)/α-Fe_2O_3 hybrids. The FTIR spectra of MIL-100(Fe)/α-Fe_2O_3-15 and MIL-100(Fe)/α-Fe_2O_3-30 in Fig. 1(b) showed bands at 710, 760, and 1380–1630 cm^{-1}, which were consistent with those of MIL-100(Fe) reported in the previous research. The band at 570 cm^{-1} of MIL-100(Fe)/α-Fe_2O_3-15 were attributed to the characteristic peak of α-Fe_2O_3 [25]. The characteristic peak of α-Fe_2O_3 in FTIR was not detected in the MIL-100(Fe)/α-Fe_2O_3-30 hybrid due to the relatively low content of α-Fe_2O_3. In general, the adsorption capacity of porous materials is related to their specific surface area and pore structure. Fig. 1(c), (d) and Fig. S(1) showed the N_2 adsorption–desorption isotherms and the pore size distribution of the as-prepared samples. The N_2 adsorption–desorption isotherms of the samples were type-IV adsorption curves, except for α-Fe_2O_3, which exhibited a type-I adsorption curve. As shown in Table 1, the BET specific surface areas of α-Fe_2O_3, MIL-100(Fe)/α-Fe_2O_3-15, MIL-100(Fe)/α-Fe_2O_3-30 and MIL-100(Fe), were 23 $m^2\ g^{-1}$, 763 $m^2\ g^{-1}$, 1138 $m^2\ g^{-1}$ and 1270 $m^2\ g^{-1}$, respectively. Though exhibiting smaller BET-SSA

Table 1
The BET specific surface area and average pore diameters of the as-prepared samples.

Sample	α-Fe_2O_3	MIL-100(Fe)/α-Fe_2O_3-15	MIL-100(Fe)/α-Fe_2O_3-30	MIL-100(Fe)
S_{BET} ($m^2\ g^{-1}$)	23	763	1138	1270
Average pore diameter (nm)	19.35	4.09	3.39	2.76

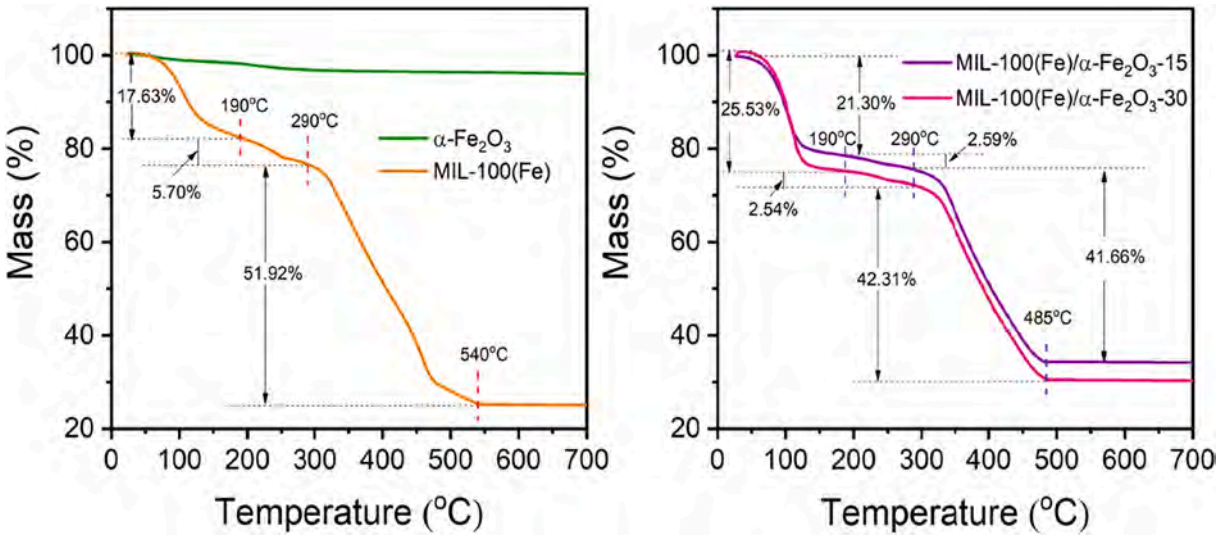

Fig. 2. TG curves of α-Fe_2O_3, MIL-100(Fe)/α-Fe_2O_3-15, MIL-100(Fe)/α-Fe_2O_3-30 and MIL-100(Fe).

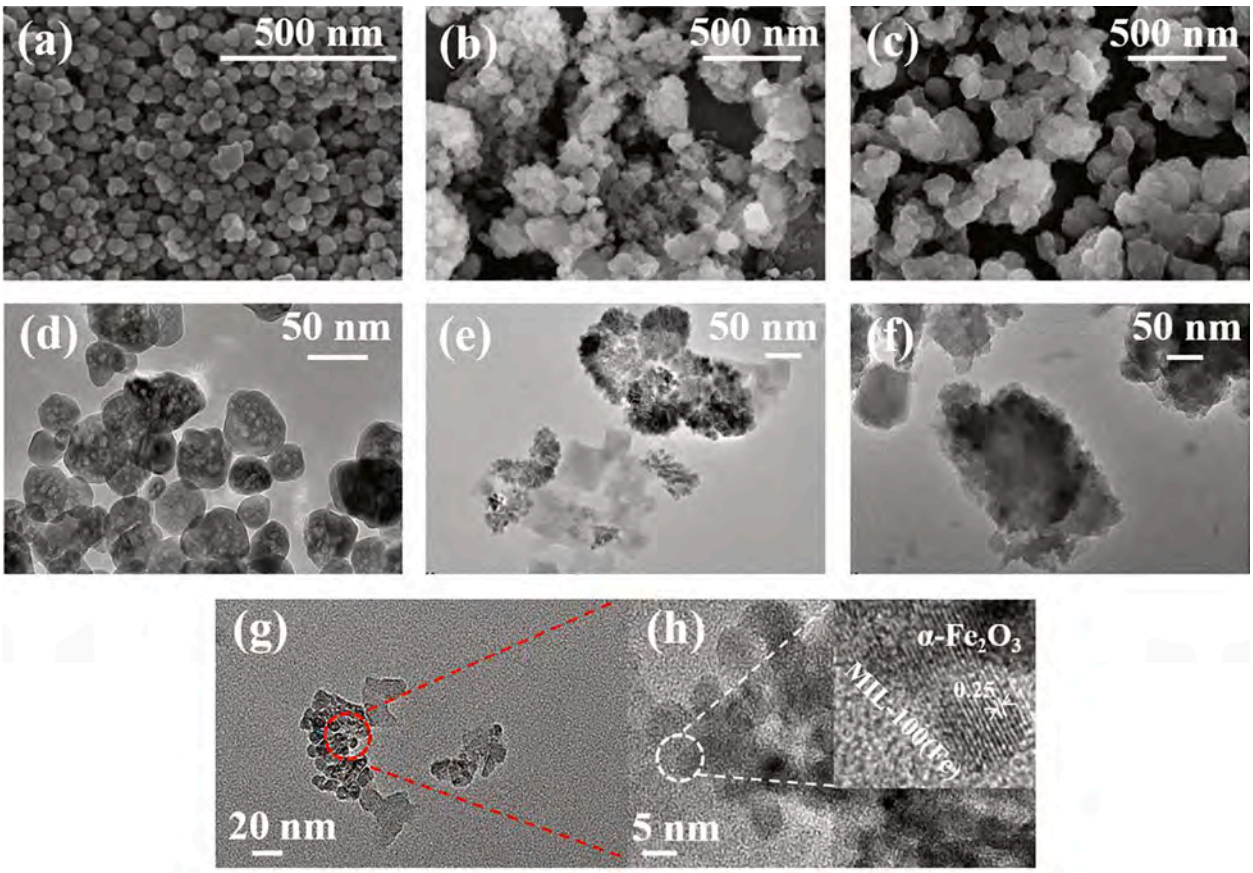

Fig. 3. The SEM images of (a) α-Fe_2O_3, (b) MIL-100(Fe)/α-Fe_2O_3-15 and (c) MIL-100(Fe); The TEM images of (d) α-Fe_2O_3, (e, g) MIL-100(Fe)/α-Fe_2O_3-15 and (f) of MIL-100(Fe); (h) The HRTEM image of MIL-100 (Fe)/α-Fe_2O_3-15.

compared with pristine MIL-100(Fe), the composites showed higher average pore diameters of 4.09 nm for MIL-100(Fe)/α-Fe_2O_3-15 and 3.39 nm for MIL-100(Fe)/α-Fe_2O_3-30 than MIL-100(Fe). The relative larger pore size could facilitate the efficient mass transfer of o-xylene and provide more accessible active sites for the absorption and degradation of o-xylene (theoretical size = 0.306 nm).

Thermogravimetric tests were carried out to analyze the composition of MIL-100(Fe)/α-Fe_2O_3 hybrids. As displayed in Fig. 2, three weight loss stages are observed over the TG curve of MIL-100(Fe) at temperature ranging from room temperature to 700 °C. The first weight loss (~17.63%) below 190 °C was related to the desorption of guest H_2O molecules inside the pores and the weight loss of 5.70 wt% in the range of 190 ~ 290 °C was attributed to the removal of coordinated H_2O molecules [26,27]. Similarly, the TG curves of MIL-100(Fe)/α-Fe_2O_3 composites also showed three weight losses. However, the first weight loss of MIL-100(Fe)/α-Fe_2O_3-15 (~21.30%) and MIL-100(Fe)/α-Fe_2O_3-

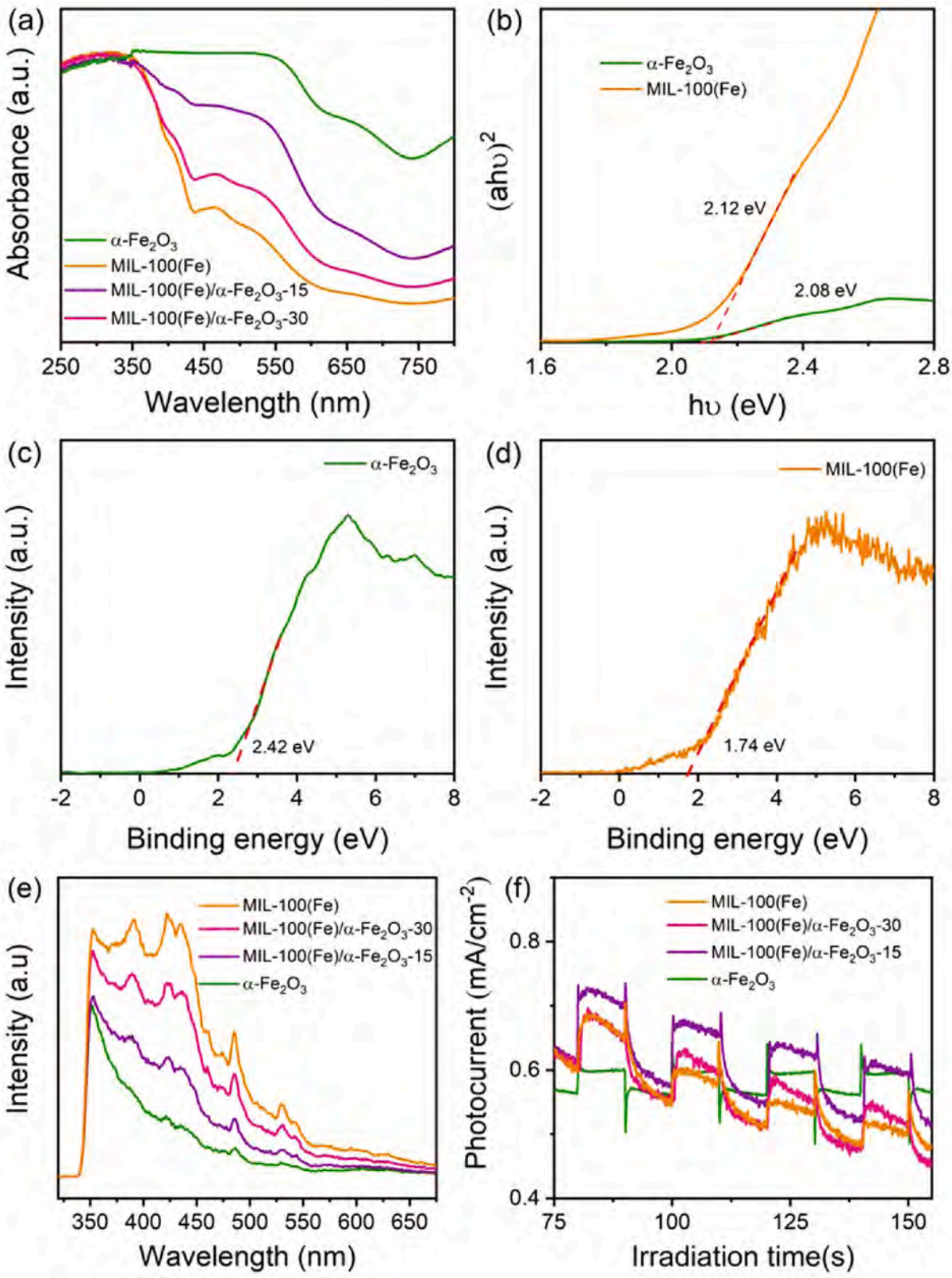

Fig. 4. (a) Diffuse reflectance spectroscopy, (b) The converted Tauc plot of $(\alpha h\nu)^2$ versus photon energy ($h\nu$), The estimated XPS valence band spectra of (c) α-Fe_2O_3 and (d) MIL-100 (Fe), (e) Photoluminescence spectra and (f) Photocurrent response of α-Fe_2O_3, MIL-100(Fe)/α-Fe_2O_3-15, MIL-100(Fe)/α-Fe_2O_3-30 and MIL-100(Fe).

30 (~25.53%) at 190 °C was higher than that of MIL-100(Fe), while the second weight loss of MIL-100(Fe)/α-Fe_2O_3-15 (~2.59%) and MIL-100 (Fe)/α-Fe_2O_3-30 (~2.54%) at 290 °C was lower compared with MIL-100 (Fe). As the temperature further increases to 540 and 485 °C, dramatic weight losses of 51.92, 41.66 and 42.31% were observed for MIL-100 (Fe), MIL-100(Fe)/α-Fe_2O_3-15 and MIL-100(Fe)/α-Fe_2O_3-30, respectively. The weight loss is related to the combustion of the BTC^{3-} and the collapse of the MIL-100(Fe) skeleton, leaving Fe_2O_3 as the residual [27].

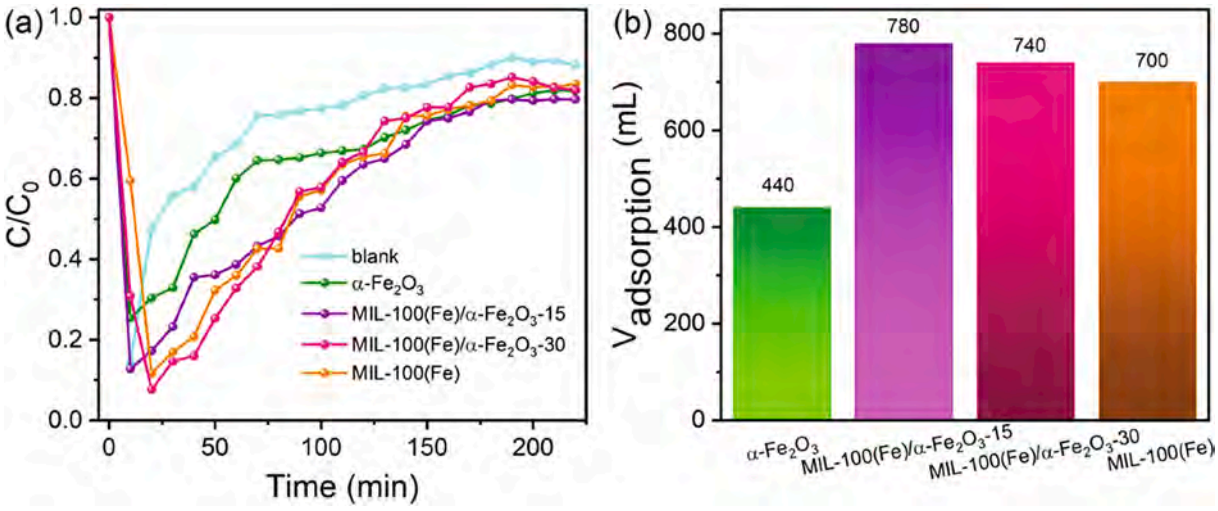

Fig. 5. (a) Adsorption curves of flowing gaseous o-xylene molecules for different samples in dark condition (b) The saturated adsorption of 0.095 g as-prepared materials for gaseous o-xylene (25 ppm).

The pattern of weight loss over MIL-100(Fe)/α-Fe_2O_3 hybrids were comparable to that of the MIL-100(Fe) sample, revealing both of them are thermally stable below 290 °C. The mass content of α-Fe_2O_3 in the final samples were determined to be 12.9 wt% for MIL-100(Fe)/α-Fe_2O_3-15 and 6.5 wt% for MIL-100(Fe)/α-Fe_2O_3-30. These results confirmed the successful control over the composition of MIL-100(Fe)/α-Fe_2O_3 hybrids through the one-step hydrothermal process.

Fig. 3 gives the micro-morphology of the samples. Ellipsoidal particles of α-Fe_2O_3 (Fig. 3(a)) and small hexagonal MIL-100(Fe) nanoparticles (Fig. 3(c)) are obtained through our hydrothermal method, quite similar with the ones reported previously [10]. Unlike the ellipsoidal nanoparticles with diameters around 50 nm observed in α-Fe_2O_3 (Fig. 3(a) and (d)), the α-Fe_2O_3 nanoparticles in MIL-100(Fe)/α-Fe_2O_3-15 (Fig. 3(e), (g) and Fig. S(2)) are much smaller with a lateral dimension of about 5 nm (Fig. 3(h)). Benefiting from the *in-situ* hydrothermal process, these α-Fe_2O_3 particles are highly dispersed and closely contact with the MIL-100 (Fe) matrix.

Based on the results above, the synthesis mechanism of MIL-100(Fe)/α-Fe_2O_3 is proposed. When adding $Fe(NO_3)_3{\cdot}9H_2O$ into deionized (DI) water at ambient temperature, the hydrolysis of Fe(III) happened and resulted in a yellow-colored solution due to the formation of monomeric octahedral $[Fe(OH)_n(H_2O)_{6-n}]^{(3-n)+}$. The further condensation of $[Fe(OH)_n(H_2O)_{6-n}]^{(3-n)+}$ led to the formation of trinuclear clusters with a triangular arrangement of Fe(III) atoms bridged by μ_3-O^{2-} ions. With the elongation of the stirring time, BTC^{3-} ions were gradually released from H_3BTC. The exchange between O^{2-} and carboxylic groups from free BTC^{3-} ions resulted in the formation of super-tetrahedra $[Fe_3(\mu_3\text{-}O)(OH)(C_6H_4(CO_2)_3)_2(H_2O)_2]$ trimers, which is the primary building unit of MIL-100(Fe) [28]. Due to the slow dissolution and protonation rate of H_3BTC in water, the degree of the replacement increases with the stirring time. When the stirring time reached one hour, the $[Fe(OH)_n(H_2O)_{6-n}]^{(3-n)+}$ trimers were completely turned into $[Fe_3(\mu_3\text{-}O)(OH)(C_6H_4(CO_2)_3)_2(H_2O)_2]$ trimers. The subsequent hydrothermal process can make these primary building units (PBUs) self-assemble into crystallized MIL-100(Fe) particles. However, when the mixing times is not sufficient for the complete conversion from $[Fe(OH)_n(H_2O)_{6-n}]^{(3-n)+}$ trimers to $[Fe_3(\mu_3\text{-}O)(OH)(C_6H_4(CO_2)_3)_2(H_2O)_2]$ trimers, these trimers may turn into $Fe(OH)_3$ during the hydrothermal process and finally resulted in the formation of Fe_2O_3 nanoparticles. Therefore, the α-Fe_2O_3 content in the MIL-100(Fe)/α-Fe_2O_3 hybrids could be well tuned by controlling the coordination of Fe(III) through adjusting the stirring time. On one hand, these Fe_2O_3 nanoparticles would work as nucleation centers for the deposition and growth of MIL-100(Fe) particles and led to the MIL-100(Fe)/α-Fe_2O_3 composites with α-Fe_2O_3 particles embedded in the MIL-100(Fe) matrix. On the other hand, the lower concentration of $[Fe(OH)_n(H_2O)_{6-n}]^{(3-n)+}$ in the solution and the reduced pH value of the solution due to the protonation of H_3BTC influence the growth of α-Fe_2O_3 and caused the formation of relatively small nanoparticles. Besides, the self-assemble of PBUs also limited the growth of α-Fe_2O_3 nanoparticles.

In order to survey the elemental composition and binding position of MIL-100(Fe)/α-Fe_2O_3 hybrids, X-ray photoelectron spectroscopy (XPS) measurement was employed to research the sample of MIL-100(Fe)/α-Fe_2O_3-15. As shown by the survey spectrum in Fig. S3(a), the C, Fe and O elements were confirmed in the MIL-100 (Fe)/α-Fe_2O_3-15 hybrid. The Fe 2p spectrum was divided into two clearly defined peaks of Fe 2p3/2 and Fe 2p1/2 (Fig. S3(b)) at the binding energies of 711.6 and 725.4 eV, which was ascribed to the Fe(III) in MIL-100(Fe)/α-Fe_2O_3-15 [29]. The C 1s spectrum showed three characteristic peaks in Fig. S3(c), related to C–C of the benzene ring (285.0 eV), C-O (286.5 eV) and C = O (289.0 eV) of carboxylic functional group. The high resolution of O 1s spectra were separated into three distinct peaks at binding energies of 530.3, 531.9 and 533.4 eV in Fig. S3(d), which were associated with oxygen element in the Fe-O, C-O and C = O of BTC^{3-} ligands, respectively.

The photo-response range is one of the important factors affecting the performance of photocatalysts [30]. The optical property of the samples was studied by UV–vis diffuse reflectance spectroscopy (DRS) as shown in Fig. 4(a). MIL-100(Fe) presented strong UV absorption with a main peak at 300 nm, which should be ascribed to the absorption resulted from ligand-to-metal charge transfer (LMCT) of O(II) to Fe(III) [31]. Moreover, the bands at the range of 300–600 nm could be originated from the spin-allowed d-d transition ($[^6A_{1g} => {}^4A_{1g} + {}^4Eg\ (G)]$) of Fe(III) in MOFs [32]. When introducing ultrafine α-Fe_2O_3 nanoparticles through *in-situ* growth, the absorption bands of MIL-100(Fe) gradually red shifted and covered both the ultraviolet and visible light regions. The converted Tauc plots versus photon energy ($h\nu$) were presented in Fig. 4 (b). The bandgap values of MIL-100(Fe) and α-Fe_2O_3 were calculated as 2.12 eV and 2.08 eV, respectively. X-ray photoelectron spectroscopy was employed to analyze the valence band structure of α-Fe_2O_3 and MIL-100 (Fe) [19]. As shown in Fig. 4(c) and 4(d) the valence band values of α-Fe_2O_3 and MIL-100(Fe) were 2.42 and 1.74 eV, respectively. According to the empirical formula ($E_{CB} = E_{VB} - E_g$, where E_{CB} is the conduction band (CB) energy, E_g is the band gap and E_{VB} is the valence band (VB) energy), the E_{CB} of α-Fe_2O_3 and MIL-100(Fe) were calculated as 0.34 and −0.38 eV, respectively. Photoluminescence spectra of the samples are compared to analyze the separation of charge carriers. The emission intensity for MIL-100(Fe)/α-Fe_2O_3-15 and MIL-100(Fe)/α-Fe_2O_3-30 was much lower (Fig. 4(e)) compared with MIL-100(Fe), indicating a much

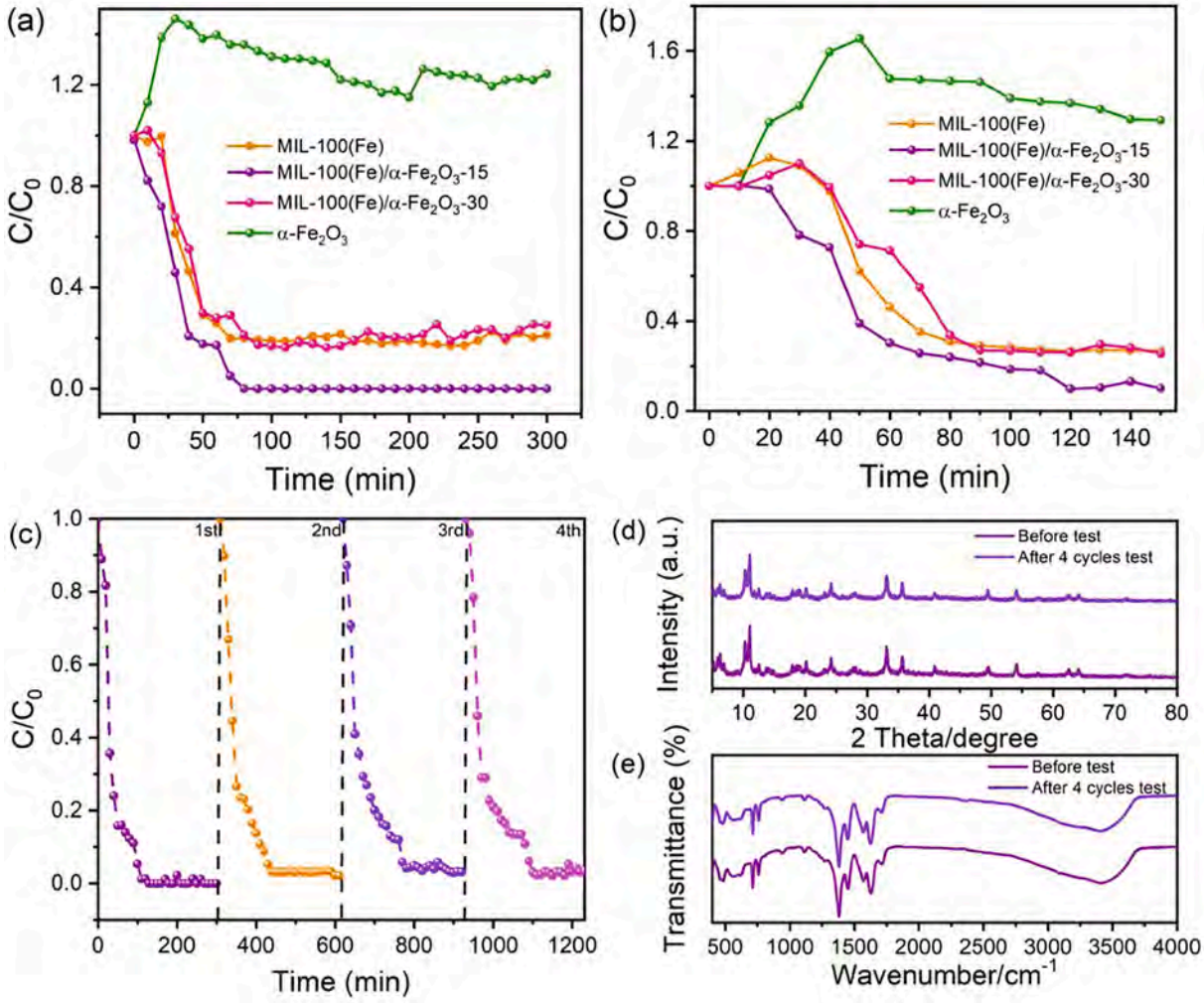

Fig. 6. Photocatalytic degradation efficiency of the as-prepared samples (a) under 250 W Xe lamp and (b) 250 W Xe lamp with filter, $\lambda \geq 420$ nm (c) Durability of MIL-100(Fe)/α-Fe_2O_3-15 for 4 repeated cycles of the integrated process under 250 W Xe lamp (d) XRD pattern and (e) FTIR spectra of the MIL-100(Fe)/α-Fe_2O_3-15 sample before and after 4 cycling tests under 250 W Xe lamp.

lower recombination efficiency of photogenerated electron–hole pairs in the MIL-100(Fe)/α-Fe_2O_3 hybrids. The formation of heterojunction between MIL-100(Fe) and α-Fe_2O_3 in the composites enabled the space separation of photon-generated electron-hole pair, which would benefit the generation of active radicals and the PCO of pollutants. The photocurrent curves for α-Fe_2O_3, MIL-100(Fe), MIL-100(Fe)/α-Fe_2O_3-15 and MIL-100(Fe)/α-Fe_2O_3-30 were displayed in Fig. 4(f). The photocurrent of all samples displayed repeatable signals in the case of light on–off switch, indicating the semiconductor characteristics of α-Fe_2O_3 and MIL-100(Fe). It could be observed that the MIL-100(Fe)/α-Fe_2O_3-15 sample shows stronger photocurrent response than MIL-100(Fe)/α-Fe_2O_3-30. The photocurrent intensity of the composites is higher with respect to pure α-Fe_2O_3 and MIL-100 (Fe) under xenon light, which can be associated with more efficient separation of photoexcited electron-hole pairs and much faster interfacial charge transfer of the composites.

3.2. Adsorption capacity of catalysts to gaseous o-xylene

The effective capture of small organic molecules is a significant prerequisite for photocatalytic degradation of gaseous pollutants. Fig. 5 (a) gives the adsorption of gaseous o-xylene on the as-prepared materials. Compared with the blank chamber, the concentration of o-xylene decreased when the samples were applied during the whole adsorption period due to the adsorption of o-xylene on these photocatalysts. According to Fig. 5(a), at a constant volume flow rate, the α-Fe_2O_3, MIL-100(Fe)/α-Fe_2O_3-15, MIL-100(Fe)/α-Fe_2O_3-30 and MIL-100(Fe) took nearly equal time to reach the adsorption equilibrium. The saturated absorbance of o-xylene gas ($V_{adsorption}$) was calculated by the following equation reported in previous literature [21,33],

$$V_{adsorption} = \left(\int_0^t v \times c_t dt\right)_{blank} - \left(\int_0^t v \times c_t dt\right)_{sample} = v\left\{\left(\int_0^t c_t dt\right)_{blank} - \left(\int_0^t c_t dt\right)_{sample}\right\}$$

υ and c_t stand for the flow rate of the mixed gas and the real-time concentration of o-xylene in the sealed cuboid glass vessel, respectively. The closed region between the curve and baseline $C/C_0 = 1$ represents the amount of o-xylene adsorbed on the surface of photocatalysts. MIL-100(Fe), MIL-100(Fe)/α-Fe_2O_3-15 and MIL-100(Fe)/α-Fe_2O_3-30 all displayed considerable adsorption capacity in Fig. 5(b) attributed to their high specific surface area and the π-π strong interaction between the organic linker BTC^{3-} and o-xylene molecules [34]. Interestingly, the amount of o-xylene absorbed slightly increased with the α-Fe_2O_3 content, which was contrary to the change in the BET SSA of the samples. The phenomenon was mainly due to the increase in the pore size enabled the smoother migration of o-xylene molecules in the channels of MOFs and the exposure of more Lewis acidic active sites for

Table 2
Comparison of photocatalytic activity of degradation of different catalysis in gas phase o-xylene (with concentration of 25 ppm) phase in the same test equipment.

Catalysts	Light Source		Catalyst dosage	Degradation Efficiency of o-xylene	Ref.
	Xe lamp	Visible light (λ > 420 nm)			
MIL-100(Fe)/α-Fe_2O_3-15	250 W		95 mg	100%	This Work
MIL-100(Fe)/α-Fe_2O_3-15		250 W	95 mg	90%	This Work
Er-doped TiO_2	400 W		100 mg	80%	[6]
rGO-TiO_2	200 W		100 mg	55%	[33]
Fe_2O_3/TiO_2	260 W		100 mg	91%	[35]
phosphoric acid modified TiO_2	300 W		100 mg	91%	[36]
Tm-doped TiO_2	400 W		100 mg	93%	[37]
carbon quantum dots (CQDs) modified TiO_2	400 W		100 mg	87%	[7]

the capture of o-xylene molecules.

3.3. Photocatalytic activity of catalysts to gaseous o-xylene

The photocatalytic activity was evaluated by comparing the removal ratio of gaseous o-xylene (Fig. 6(a) and 6(b)) under two light sources. Interestingly, the amount of o-xylene showed an increase when α-Fe_2O_3 and TiO_2 (Fig. S4) were light irradiated. The phenomenon was attributed to the thermal-induced desorption of o-xylene molecules adsorbed on the photocatalyst and the wall of the reaction chamber under light irradiation, which could not be degraded by the catalyst in time. Similar phenomenon was observed in the blank experiment where no catalyst was applied (Fig. S5). MIL-100(Fe) exhibited an activity toward o-xylene removal with efficiency up to 80% and 75% under 250 W Xe lamp light irradiation and visible light, respectively. The o-xylene removal efficiency further increased to 100% and remained stable for 300 min under Xenon light when applying MIL-100(Fe)/α-Fe_2O_3-15 as the photocatalyst, which was in accordance with its high specific surface area, lower PL intensity and high photo-currency. Besides, the MIL-100(Fe)/α-Fe_2O_3-15 also exhibited promising photocatalytic activity under visible light with an o-xylene removal ratio of 90%, which was much higher compared to traditional photocatalysts (Table 2 and Fig. S(4)). The MIL-100(Fe)/α-Fe_2O_3-30 hybrid displayed a slightly lower activity towards the PCO of o-xylene, but still comparable to MIL-100(Fe), which

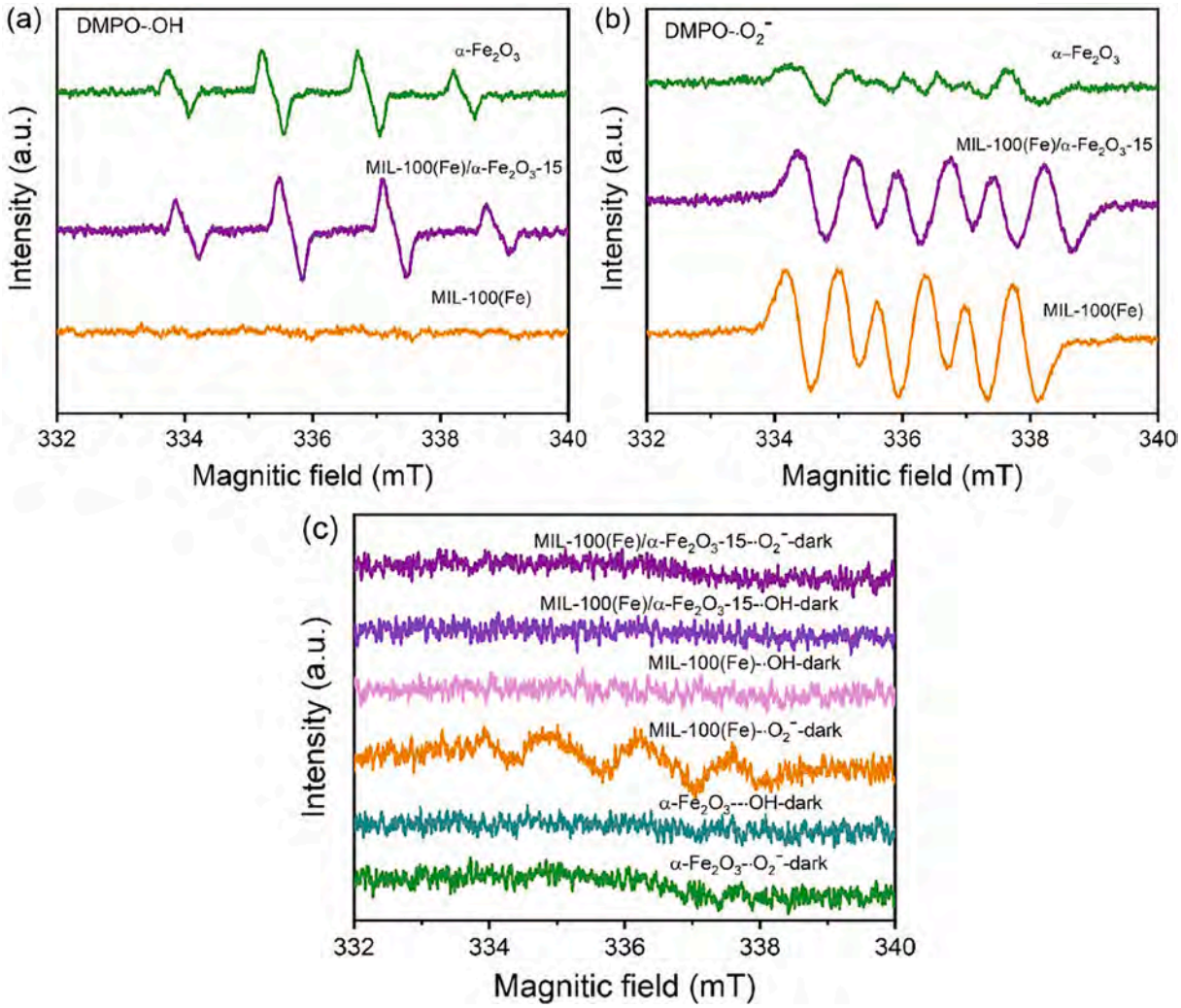

Fig. 7. (a) DMPO spin-trapping ESR spectra for the •OH of α-Fe_2O_3, MIL-100(Fe), and MIL-100(Fe)/α-Fe_2O_3-15 (in aqueous for DMPO− •OH) (b) DMPO spin-trapping ESR spectra for the $\bullet O_2^-$ of α-Fe_2O_3, MIL-100(Fe), and MIL-100(Fe)/α-Fe_2O_3-15 (in ethanol for DMPO− $\bullet O_2^-$) (c) DMPO spin-trapping ESR spectra of α-Fe_2O_3, MIL-100 (Fe), and MIL-100(Fe)/α-Fe_2O_3-15 hybrid without light irradiation.

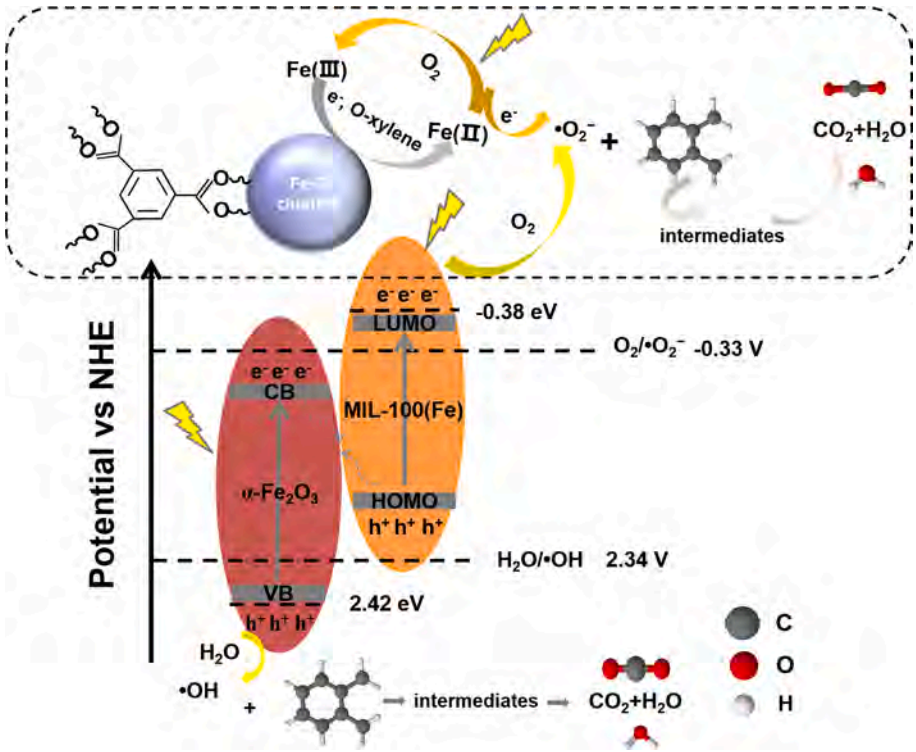

Scheme 1. Direct Z-scheme mechanism in MIL-100(Fe)/α-Fe_2O_3 hybrid.

was probably due to the lower α-Fe_2O_3 content (6.5 wt%). We further verified the durability of MIL-100(Fe)/α-Fe_2O_3-15 by repeating the integrated adsorption and degradation steps (Fig. 6(c)). The photocatalyst remained stable after 4 cycles under 250 W Xe lamp light irradiation with removal efficiency as high as 96%. No obvious change was observed in the XRD and FTIR spectra of MIL-100(Fe)/α-Fe_2O_3-15 before and after the cyclic tests (Fig. 6(d) and 6(e)), indicating its stability as an appliable photocatalyst.

3.4. The mechanism of PCO of o-xylene

In the purpose of understanding the excellent PCO performance of MIL-100(Fe)/α-Fe_2O_3 composites, ESR spin-trapping was deployed to detect the generation of transient free radicals [18]. Fig. 7(a) gives the signal of DMPO-•OH with four peaks whose intensities of standard ratios were 1:2:2:1 and Fig. 7(b) shows the six characteristic peaks of DMPO-$•O_2^-$ with identical intensity. Both signals of •OH and $•O_2$ were detected for MIL-100(Fe)/α-Fe_2O_3-15 while α-Fe_2O_3 only gave signals for •OH radicals and pure MIL-100(Fe) only gave signals for $•O_2^-$ radicals. The intensity ESR-signals for both •OH and $•O_2^-$ radicals generated by MIL-100(Fe)/α-Fe_2O_3-15 were comparable with pure α-Fe_2O_3 and MIL-100 (Fe). In contrast, no signal was detected under dark for any of the samples (Fig. 7(c)). These results of radical spin-trapping indicated a Z-scheme structure was formed in the MIL-100(Fe)/α-Fe_2O_3-15 hybrid instead of a p–n heterojunction. In the case of p–n heterojunctions, the photoexcited electrons in the CB of MIL-100(Fe) would incline to transfer to the CB of α-Fe_2O_3, and the holes in the VB of α-Fe_2O_3 would be transferred to the VB of MIL-100(Fe). In view of the fact that the E_{VB} (1.74 eV) of MIL-100(Fe) was lower than the standard potential energy for the generation of •OH (2.34 V) through the oxidation of H_2O (H_2O +

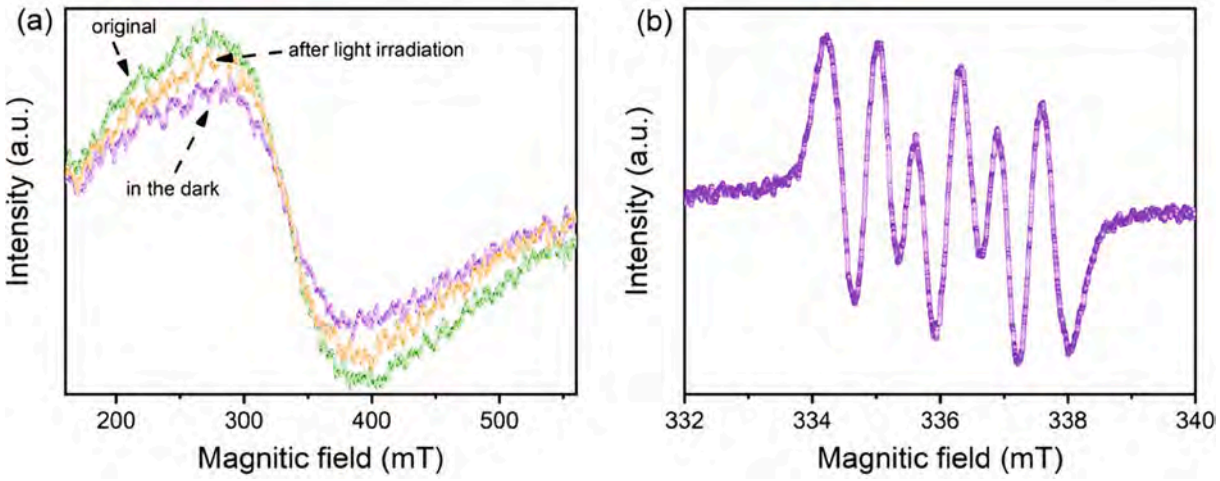

Fig. 8. (a) ESR spectra of MIL-100(Fe)/α-Fe_2O_3-15 after adsorption of o-xylene in the dark and upon irradiation (b) DMPO spin-trapping ESR spectra for the $•O_2^-$ radical in the presence of MIL-100(Fe)/α-Fe_2O_3-15 after adsorption of o-xylene under irradiation.

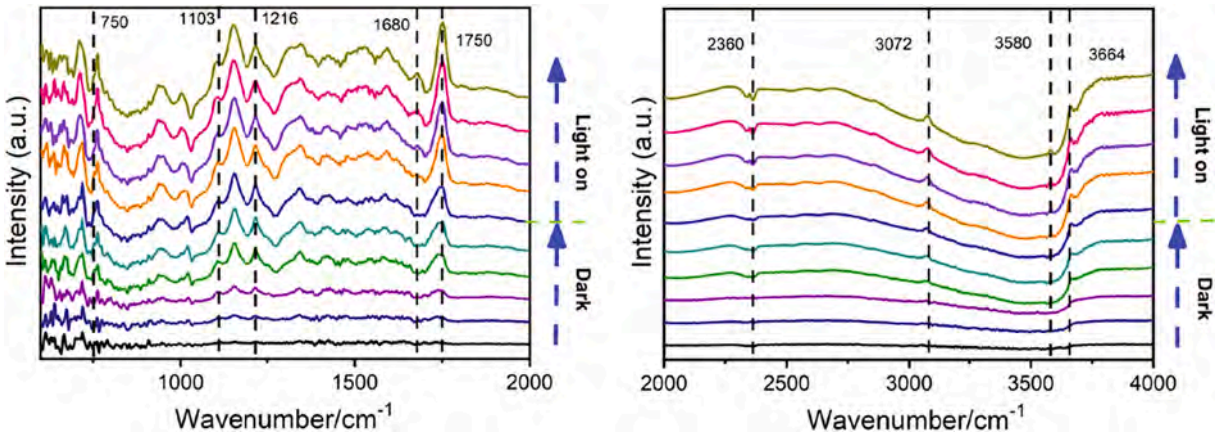

Fig. 9. DRIFT spectra of absorption and degradation process for gaseous o-xylene over the MIL-100(Fe)/α-Fe_2O_3-15.

$h^+_{VB} \rightarrow \bullet OH + H^+$) and the energy of electrons in the CB ($E_{CB} = 0.34$ eV) of α-Fe_2O_3 was not sufficient for the reduction of O_2 to $\bullet O_2^-$ ($O_2 + e^- \rightarrow \bullet O_2^-$, −0.33 V), almost no •OH nor $\bullet O_2^-$ could be generated. Therefore, the Z-type charge transfer mechanism was applied to illustrate the excellent performance of MIL-100(Fe)/α-Fe_2O_3-15.

The band alignment between α-Fe_2O_3 and MIL-100(Fe) lead to the formation of the Z-scheme structure, which was supposed to play a key role in enhancing the photocatalytic activity of MIL-100(Fe)/α-Fe_2O_3-15 toward o-xylene removal. As shown by Scheme 1, both α-Fe_2O_3 and MIL-100(Fe) can be excited by light to generate holes and electrons. The electrons generated at the conduction band of α-Fe_2O_3 directly moved through the tight interface between α-Fe_2O_3 and MIL-100(Fe) and recombined with holes at the valence band of MIL-100(Fe). Electrons generated at the conduction band of MIL-100(Fe) can efficiently migrate to the surface and participate in $\bullet O_2^-$ generation, while holes generated in the VB of α-Fe_2O_3 can be maximally utilized in H_2O oxidation to generate •OH. Such a Z-type channel for electron transfer significantly extended the lifetime of active electrons and holes with strong reduction and oxidizing capability and promoted the generation of reactive $\bullet O_2^-$ and •OH radicals, which were essential for the improved photocatalytic degradation of o-xylene performance.

Interestingly, though capable of generating •OH radicals, almost no o-xylene removal was observed for Fe_2O_3. This phenomenon could be attributed to the reason. This mismatch between ESR test and photocatalytic performance of α-Fe_2O_3 shows that the ESR results obtained in the liquid phase may not reflect the actual situation under gas phase conditions. The accurate characterization of reactive radicals in the gas phase would be important for the future work in the photocatalytic degradation of gaseous pollutants.

The change of Fe(III) ions during the photocatalytic reaction was analyzed through ESR tests to further understand the reaction mechanism [38,39]. As shown in Fig. 8(a), the ESR signal corresponding to Fe (III) in the MIL-100(Fe)/α-Fe_2O_3-15 sample firstly decreased during the adsorption of o-xylene and then increased after turning on the Xe light, implying a depletion of Fe(III) during the adsorption period and then a supplement of Fe(III) ions under light irradiation. In the meantime, $\bullet O_2^-$ radicals were detected in the ESR spectra of MIL-100(Fe)/α-Fe_2O_3-15 obtained in liquid o-xylene under light irradiation conditions (Fig. 8(b)), indicating the oxidation by oxygen might be the key reason for the increase of Fe(III).

The photocatalytic degradation process of o-xylene was also investigated by monitoring the adsorbed species on MIL-100(Fe)/α-Fe_2O_3-15 hybrid with *in-situ* DRIFTS. The reaction was carried out in a mixed flow of o-xylene and air at room temperature. The infrared background peak of the MIL-100(Fe)/α-Fe_2O_3-15 hybrid was subtracted before the reaction proceeding. Fig. 9 showed the DRIFTS spectra of adsorbed species on the catalysts during adsorption–desorption and photocatalytic degradation process. Generally, the bands at 3072 cm^{-1}, 1450–1600 cm^{-1}, 720–750 cm^{-1} could be assigned to the stretching vibration ($\nu_{=C-H}$), the skeleton vibration ($\nu_{C=C}$) and *ortho*-substitution of benzene ring [40,41]. Phenol (1103–1216 cm^{-1}) [41–43], free hydroxyl (3664 cm^{-1}) and carbon dioxide (2340–2360 cm^{-1}) [40,44] were detected during the adsorption process without light irradiation (Fig. 9). As the adsorption proceeded, increased accumulation of these intermediates was observed, which indicated that the o-xylene oxidation can take place at ambient temperature without light irradiation [45]. After the adsorption equilibrium was reached, DRIFT spectra of the photocatalytic decomposition of o-xylene on MIL-100(Fe)/α-Fe_2O_3-15 was collected under Xenon light irradiation. As shown in Fig. 9, the peak at 750 cm^{-1} (*ortho*-substitution) gradually disappeared, implying that the methyl substituent of o-xylene was oxidized. The hydroxyl radicals generated under the irradiation of Xenon light attacked the side chain methyl group of o-xylene, resulting in the disappearance of the peak at 750 cm^{-1}, and the increase in the peak intensity of phenol (1103–1216 cm^{-1}) and benzaldehyde (1680 cm^{-1}) [46,47]. The peaks for esters (1750 cm^{-1}) [40,48] increased due to the rapid dehydration of organic carboxylic acid and alcohol or phenol groups on the Lewis acid sites. It was worth noting that the intensity of the characteristic peaks, including free water (3580 cm^{-1}) and carbon dioxide (2340–2360 cm^{-1}) gradually increased, implying that o-xylene were rapidly oxidized into CO_2 and water, which were then adsorbed on the surface of MIL-100(Fe)/α-Fe_2O_3-15. The variety of relative humidity in the reaction chamber in the process of photocatalytic degradation of o-xylene and the CO_2 concentration detected after the process of photocatalytic degradation of o-xylene were shown in Fig. S6(a) and (b), respectively. These results combined with *in-situ* DRIFTS analysis indicated that o-xylene molecules were finally mineralized into CO_2 and H_2O.

On the basis of the above results, we proposed the mechanism shown by Scheme 1 for the photocatalytic degradation of o-xylene on MIL-100 (Fe)/α-Fe_2O_3-15. Firstly, o-xylene was absorbed by MIL-100(Fe)/α-Fe_2O_3-15 under dark condition. The reduction of Fe(III) in the Fe-O clusters would happen due to the charge transfer between Fe(III) and absorbed o-xylene molecules and resulted in the depletion of Fe(III) and the formation of Fe(II) [49]. The irradiation of light is important for the activation of O_2 and the oxidation of Fe(II) to Fe(III), which was faster compared with the reduction of Fe(III) by absorbed species [50]. This reaction led to the increase in the ESR intensity for Fe(III) and the generation of $\bullet O_2^-$ radicals, which would then participate in the oxidation of o-xylene. However, the ESR intensity for Fe(III) after the light irradiation was still lower compared with original sample, which may be due to the excitation and transfer of electrons from linkers to Fe_3-μ$_3$-oxo clusters [51]. Besides, the irradiation of light would also cause the excitation of both MIL-100(Fe) and α-Fe_2O_3 in the MIL-100(Fe)/α-Fe_2O_3 hybrid. The photon-induces electrons and holes would transfer between

the two components following the Z-scheme channels and react with absorbed water and oxygen to generate $\bullet O_2^-$ and •OH radicals. Absorbed o-xylene molecules would then be oxidized to CO_2 and water by these radicals.

4. Conclusion

In summary, Z-scheme MIL-100(Fe)/α-Fe_2O_3 hybrid photocatalysts was synthesized through a facile one-step hydrothermal method for the PCO of gas o-xylene. Among the samples, the MIL-100(Fe)/α-Fe_2O_3-15 exhibits excellent photocatalytic activity toward o-xylene removal, with a degradation efficiency of 100% and 90% under the irradiation of 250 W Xenon light and visible light ($\lambda \geq 420$ nm). The enhanced performance of o-xylene removal in MIL-100(Fe)/α-Fe_2O_3-15 was attributed to the high SSA, suitable pore structure and tight connection between α-Fe_2O_3 and MIL-100(Fe) formed during the hydrothermal process, which enabled the formation of Z-scheme heterojunction structure. The interface between α-Fe_2O_3 and MIL-100(Fe) enables the fast electron transfer from the conduction band of α-Fe_2O_3 to the valence band of MIL-100 (Fe), leaving holes in the valence band to oxidize adsorbed H_2O to generate highly active •OH radicals and electrons in the conductive band of MOF for the generation of active $\bullet O_2^-$ species. The electron-hole recombination in both α-Fe_2O_3 and MIL-100(Fe) are suppressed, which further benefit the generation of active radicals. In addition, the reversible conversion between Fe(III) and Fe(II) under light irradiation was confirmed to be essential for the PCO of o-xylene. This study provides a novel Z-scheme MIL-100(Fe)/α-Fe_2O_3 composite photocatalyst for the effective decomposition of o-xylene. We believed that this paper would shed light on the design and application of MOFs-based photocatalysts in the PCO of gaseous organic pollutants.

Declaration of Competing Interest

The authors declare that they have no known competing financial interests or personal relationships that could have appeared to influence the work reported in this paper.

Acknowledgment

This work was financially supported by the National Key Research and Development Program of China (2016YFA0203000), National Natural Science Foundation of China (52072387), Shanghai Commission of Science and Technology Program (19DZ1202600, 20DZ1204100), the National Natural Science Foundation of China (41907303, 51574205), the State Key Laboratory Director Fund of SICCAS (Y9ZC0102), the Natural Science Foundation of Guangdong Province (2018B030311022), and the Innovative Research Team (in Science and Technology) in University of Henan Province (19IRTSTHN028).

Appendix A. Supplementary data

Supplementary data to this article can be found online at https://doi.org/10.1016/j.cej.2021.129112.

References

[1] Z. Tan, K. Lu, M. Jiang, R. Su, H. Wang, S. Lou, Q. Fu, C. Zhai, Q. Tan, D. Yue, D. Chen, Z. Wang, S. Xie, L. Zeng, Y. Zhang, Daytime atmospheric oxidation capacity in four Chinese megacities during the photochemically polluted season: a case study based on box model simulation, Atmos. Chem. Phys. 19 (6) (2019) 3493–3513, https://doi.org/10.5194/acp-19-3493-201910.5194/acp-19-3493-2019-supplement.

[2] A. Mehra, Y. Wang, J.E. Krechmer, A. Lambe, F. Majluf, M.A. Morris, M. Priestley, T.J. Bannan, D.J. Bryant, K.L. Pereira, J.F. Hamilton, A.R. Rickard, M.J. Newland, H. Stark, P. Croteau, J.T. Jayne, D.R. Worsnop, M.R. Canagaratna, L. Wang, H. Coe, Evaluation of the chemical composition of gas- and particle-phase products of aromatic oxidation, Atmos. Chem. Phys. 20 (16) (2020) 9783–9803, https://doi.org/10.5194/acp-20-9783-202010.5194/acp-20-9783-2020-supplement.

[3] M. Kask, J. Bolobajev, M. Krichevskaya, Gas-phase photocatalytic degradation of acetone and toluene, and their mixture in the presence of ozone in continuous multi-section reactor as possible air post-treatment for exhaust from pulsed corona discharge, Chem. Eng. J. 399 (2020), 125815, https://doi.org/10.1016/j.cej.2020.125815.

[4] Honda, A. Fujishima, Kenichi, Electrochemical Photolysis of Water at a Semiconductor Electrode, Nature. 238 July 7 (1972).

[5] Q. Zeng, X. Xie, X. Wang, Y. Wang, G. Lu, D.Y. Pui, J. Sun, Enhanced photocatalytic performance of Ag@TiO_2 for the gaseous acetaldehyde photodegradation under fluorescent lamp, Chem. Eng. J. 341 (2018) 83–92, https://doi.org/10.1016/j.cej.2018.02.015.

[6] Z. Rao, X. Xie, X. Wang, A. Mahmood, S. Tong, M. Ge, J. Sun, Defect Chemistry of Er^{3+}-Doped TiO_2 and Its Photocatalytic Activity for the Degradation of Flowing Gas-Phase VOCs, J. Phys. Chem. C. 123 (2019) 12321–12334, https://doi.org/10.1021/acs.jpcc.9b02093.

[7] A. Mahmood, X. Wang, G. Shi, Z. Wang, X. Xie, J. Sun, Revealing adsorption and the photodegradation mechanism of gas phase o-xylene on carbon quantum dots modified TiO_2 nanoparticles, J. Hazard. Mater. 386 (2020), 121962, https://doi.org/10.1016/j.jhazmat.2019.121962.

[8] E. Barea, C. Montoro, J.A.R. Navarro, Toxic gas removal-metal-organic frameworks for the capture and degradation of toxic gases and vapours, Chem. Soc. Rev. 43 (16) (2014) 5419–5430, https://doi.org/10.1039/C3CS60475F.

[9] T. Zurrer, K. Wong, J. Horlyck, E.C. Lovell, J. Wright, N.M. Bedford, Z. Han, K. Liang, J. Scott, R. Amal, Mixed-metal MOF-74 templated catalysts for efficient carbon dioxide capture and methanation, Adv. Funct. Mater. 31 (9) (2021) 2007624, https://doi.org/10.1002/adfm.v31.910.1002/adfm.202007624.

[10] H. Wang, P. Rassu, X. Wang, H. Li, X. Wang, X. Wang, X. Feng, A. Yin, P. Li, X. u. Jin, S.-L. Chen, X. Ma, B.o. Wang, An iron-containing metal-organic framework as a highly efficient catalyst for ozone decomposition, Angew. Chem. Int. Ed. 57 (50) (2018) 16416–16420, https://doi.org/10.1002/anie.201810268.

[11] V. Chevalier, J. Martin, D. Peralta, A. Roussey, F. Tardif, Performance of HKUST-1 Metal-Organic Framework for a VOCs mixture adsorption at realistic concentrations ranging from 0.5 to 2.5 ppmv under different humidity conditions, J. Environ Chem. Eng. 7 (2019), 103131, https://doi.org/10.1016/j.jece.2019.103131.

[12] S. Remiro-Buenamañana, M. Cabrero-Antonino, M. Martínez-Guanter, M. Álvaro, S. Navalón, H. García, Influence of co-catalysts on the photocatalytic activity of MIL-125(Ti)-NH_2 in the overall water splitting, Appl. Catal. B: Environ. 254 (2019) 677–684, https://doi.org/10.1016/j.apcatb.2019.05.027.

[13] A. Melillo, M. Cabrero-Antonino, S. Navalón, M. Álvaro, B. Ferrer, H. García, Enhancing visible-light photocatalytic activity for overall water splitting in UiO-66 by controlling metal node composition, Appl. Catal. B: Environ. l 278 (2020), 119345, https://doi.org/10.1016/j.apcatb.2020.119345.

[14] X. Li, Y. Pi, L. Wu, Q. Xia, J. Wu, Z. Li, J. Xiao, Facilitation of the visible light-induced Fenton-like excitation of H_2O_2 via heterojunction of g-C_3N_4/NH_2-Iron terephthalate metal-organic framework for MB degradation, Appl. Catal. B: Environ. 202 (2017) 653–663, https://doi.org/10.1016/j.apcatb.2016.09.073.

[15] N. Liu, W. Huang, X. Zhang, L. Tang, L. Wang, Y. Wang, M. Wu, Ultrathin graphene oxide encapsulated in uniform MIL-88A(Fe) for enhanced visible light-driven photodegradation of RhB, Appl. Catal. B: Environ. 221 (2018) 119–128, https://doi.org/10.1016/j.apcatb.2017.09.020.

[16] P. Li, S. Kim, J. Jin, H.C. Do, J.H. Park, Efficient photodegradation of volatile organic compounds by iron-based metal-organic frameworks with high adsorption capacity, Appl. Catal. B: Environ. 263 (2020) 118284, https://doi.org/10.1016/j.apcatb.2019.118284.

[17] F. Dong, Z. Wang, Y. Li, W.-K. Ho, S.C. Lee, Immobilization of Polymeric g-C_3N_4 on structured ceramic foam for efficient visible light photocatalytic air purification with real indoor illumination, Environ. Sci. Technol. 48 (17) (2014) 10345–10353, https://doi.org/10.1021/es502290f.

[18] X. She, J. Wu, H. Xu, J. Zhong, Y. Wang, Y. Song, K. Nie, Y. Liu, Y. Yang, M.-T. Rodrigues, R. Vajtai, J. Lou, D. Du, H. Li, P.M. Ajayan, High Efficiency photocatalytic water splitting using 2D α-Fe_2O_3/g-C_3N_4 Z-scheme catalysts, Adv. Energy Mater. 7 (17) (2017) 1700025, https://doi.org/10.1002/aenm.201700025.

[19] L. Liu, L. Zhang, F. Wang, K. Qi, H. Zhang, X. Cui, W. Zheng, Bi-metal–organic frameworks type II heterostructures for enhanced photocatalytic styrene oxidation, Nanoscale. 11 (16) (2019) 7554–7559, https://doi.org/10.1039/C9NR00790C.

[20] X. He, H. Fang, D.J. Gosztola, Z. Jiang, P. Jena, W.-N. Wang, Mechanistic insight into photocatalytic pathways of MIL-100(Fe)/TiO_2 composites, ACS Appl. Mater. Inter. 11 (13) (2019) 12516–12524, https://doi.org/10.1021/acsami.9b0022310.1021/acsami.9b00223.s001.

[21] X. Dai, Y. Wang, X. Wang, S. Tong, X. Xie, Polarity on adsorption and photocatalytic performances of N-GR/TiO_2 towards gaseous acetaldehyde and ethylene, Appl. Surf. Sci. 485 (2019) 255–265, https://doi.org/10.1016/j.apsusc.2019.04.221.

[22] H. Song, S. Yan, Y. Yao, L. Xia, X. Jia, J. Xu, 3D α-Fe_2O_3 nanorods arrays@graphene oxide nanosheets as sensing materials for improved gas sensitivity, Chem. Eng. J. 370 (2019) 1331–1340, https://doi.org/10.1016/j.cej.2019.03.254.

[23] P. Horcajada, S. Surblé, C. Serre, D.Y. Hong, Y.K. Seo, J.S. Chang, J.M. Grenèche, I. Margiolaki, G. Férey, Synthesis and catalytic properties of MIL-100(Fe), an iron (iii) carboxylate with large pores, Chem. Commun. (2007) 2820–2822, https://doi.org/10.1039/b704325b.

[24] M. Ahmad, S. Chen, F. Ye, X. Quan, S. Afzal, H. Yu, X. Zhao, Efficient photo-Fenton activity in mesoporous MIL-100(Fe) decorated with ZnO nanosphere for pollutants

degradation, Appl. Catal. B: Environ. 245 (2019) 428–438, https://doi.org/10.1016/j.apcatb.2018.12.057.
[25] K. Wang, M. Chen, Z. He, L.-a. Huang, S. Zhu, S. Pei, J. Guo, H. Shao, J. Wang, Hierarchical Fe_3O_4@C nanospheres derived from Fe_2O_3/MIL-100(Fe) with superior high-rate lithium storage performance, J. Alloys Compd. 755 (2018) 154–162, https://doi.org/10.1016/j.jallcom.2018.04.320.
[26] N. Tsumori, L. Chen, Q. Wang, Q.-L. Zhu, M. Kitta, Q. Xu, Quasi-MOF: Exposing Inorganic Nodes to Guest Metal Nanoparticles for Drastically Enhanced Catalytic Activity, Chem. 4 (4) (2018) 845–856, https://doi.org/10.1016/j.chempr.2018.03.009.
[27] G. Song, Z. Wang, L. Wang, G. Li, M. Huang, F. Yin, Preparation of MOF(Fe) and its catalytic activity for oxygen reduction reaction in an alkaline electrolyte, Chinese J. Catal. 35 (2) (2014) 185–195, https://doi.org/10.1016/S1872-2067(12)60729-3.
[28] Y.K. Seo, J.W. Yoon, J. Lee, U.-H. Lee, Y. Hwang, C. Jun, P. Horcajada, C. Serre, J. Chang, Large scale fluorine-free synthesis of hierarchically porous iron(III) trimesate MIL-100(Fe) with a zeolite MTN topology, Microporous Mesoporous Mater. 157 (2012) 137–145, https://doi.org/10.1016/j.micromeso.2012.02.027.
[29] X. Liu, R. Dang, W. Dong, X. Huang, J. Tang, H. Gao, G. Wang, A sandwich-like heterostructure of TiO_2 nanosheets with MIL-100(Fe): A platform for efficient visible-light-driven photocatalysis, Appl. Catal. B: Environ. 209 (2017) 506–513, https://doi.org/10.1016/j.apcatb.2017.02.073.
[30] M. Guo, Z. Xing, T. Zhao, Z. Li, S. Yang, W. Zhou, WS_2 quantum dots/MoS_2@WO_{3-x} core-shell hierarchical dual Z-scheme tandem heterojunctions with wide-spectrum response and enhanced photocatalytic performance, Appl. Catal. B: Environ. 257 (2019) 117913, https://doi.org/10.1016/j.apcatb.2019.117913.
[31] S. Bordiga, C. Lamberti, G. Ricchiardi, L. Regli, F. Bonino, A. Damin, K.-P. Lillerud, M. Bjorgen, A. Zecchina, Electronic and vibrational properties of a MOF-5 metal-organic framework: ZnO quantum dot behaviour, Chem. Commun. (20) (2004) 2300–2301, https://doi.org/10.1039/B407246D.
[32] C. Zhang, L. Ai, J. Jiang, Solvothermal synthesis of MIL-53(Fe) hybrid magnetic composites for photoelectrochemical water oxidation and organic pollutant photodegradation under visible light, J. Mater. Chem. A. 3 (6) (2015) 3074–3081, https://doi.org/10.1039/C4TA04622F.
[33] W. Lin, X. Xie, X. Wang, Y. Wang, D. Segets, J. Sun, Efficient adsorption and sustainable degradation of gaseous acetaldehyde and o-xylene using rGO-TiO_2 photocatalyst, Chem. Eng. J. 349 (2018) 708–718, https://doi.org/10.1016/j.cej.2018.05.107.
[34] W. Xiong, G. Zeng, Z. Yang, Y. Zhou, C. Zhang, M. Cheng, Y. Liu, L. Hu, J. Wan, C. Zhou, R. Xu, X. Li, Adsorption of tetracycline antibiotics from aqueous solutions on nanocomposite multi-walled carbon nanotube functionalized MIL-53(Fe) as new adsorbent, Sci. Total Environ. 627 (2018) 235–244, https://doi.org/10.1016/j.scitotenv.2018.01.249.
[35] X. Dai, G. Lu, Y. Hu, X. Xie, X. Wang, J. Sun, Reversible redox behavior of Fe_2O_3/TiO_2 composites in the gaseous photodegradation process, Ceram. Int. 45 (10) (2019) 13187–13192, https://doi.org/10.1016/j.ceramint.2019.03.255.
[36] Z. Wang, A. Mahmood, X. Xie, X. Wang, H. Qiu, J. Sun, Surface adsorption configurations of H_3PO_4 modified TiO_2 and its influence on the photodegradation intermediates of gaseous o-xylene, Chem. Eng. J. 393 (2020), 124723, https://doi.org/10.1016/j.cej.2020.124723.
[37] Z. Rao, G. Shi, Z. Wang, A. Mahmood, X. Xie, J. Sun, Photocatalytic degradation of gaseous VOCs over Tm^{3+}-TiO_2: Revealing the activity enhancement mechanism and different reaction paths, Chem. Eng. J. 395 (2020), 125078, https://doi.org/10.1016/j.cej.2020.125078.
[38] M. Nishikawa, Y. Mitani, Y. Nosaka, Photocatalytic Reaction Mechanism of Fe(III)-Grafted TiO_2 Studied by Means of ESR Spectroscopy and Chemiluminescence Photometry, J. Phys. Chem. C. 116 (28) (2012) 14900–14907, https://doi.org/10.1021/jp3020657.
[39] A. Vinu, T. Krithiga, V.V. Balasubramanian, A. Asthana, P. Srinivasu, T. Mori, K. Ariga, G. Ramanath, P.G. Ganesan, Characterization and catalytic performances of three-dimensional mesoporous FeSBA-1 catalysts, J. Phys. Chem. B. 110 (24) (2006) 11924–11931, https://doi.org/10.1021/jp061523h.
[40] Y. Wu, S. Shi, S. Yuan, T. Bai, S. Xing, Insight into the enhanced activity of Ag/NiOx-MnO_2 for catalytic oxidation of o-xylene at low temperatures, Appl. Surf. Sci. 479 (2019) 1262–1269, https://doi.org/10.1016/j.apsusc.2019.01.134.
[41] Y. Wu, S. Yuan, R. Feng, Z. Ma, Y. Gao, S. Xing, Comparative study for low-temperature catalytic oxidation of o-xylene over doped OMS-2 catalysts: Role of Ag and Cu, Mol. Catal. 442 (2017) 164–172, https://doi.org/10.1016/j.mcat.2017.09.020.
[42] X. Tang, J. Chen, Y. Li, Y. Li, Y. Xu, W. Shen, Complete oxidation of formaldehyde over Ag/MnOx–CeO_2 catalysts, Chem. Eng. J. 118 (1-2) (2006) 119–125, https://doi.org/10.1016/j.cej.2006.02.002.
[43] Y. Wu, Y. Lu, C. Song, Z. Ma, S. Xing, Y. Gao, A novel redox-precipitation method for the preparation of α-MnO_2 with a high surface Mn^{4+} concentration and its activity toward complete catalytic oxidation of o-xylene, Catal. Today. 201 (2013) 32–39, https://doi.org/10.1016/j.cattod.2012.04.032.
[44] Y.u. Xia, Z. Wang, Y. Feng, S. Xie, Y. Liu, H. Dai, J. Deng, In situ molten salt derived iron oxide supported platinum catalyst with high catalytic performance for o-xylene elimination, Catal. Today. 351 (2020) 30–36, https://doi.org/10.1016/j.cattod.2019.01.076.
[45] J. Li, W. Cui, P. Chen, X. Dong, Y. Chu, J. Sheng, Y. Zhang, Z. Wang, F. Dong, Unraveling the mechanism of binary channel reactions in photocatalytic formaldehyde decomposition for promoted mineralization, Appl. Catal. B. 260 (2020) 118130, https://doi.org/10.1016/j.apcatb.2019.118130.
[46] Z. Jia, X. Wang, F. Thevenet, A. Rousseau, Dynamic probing of plasma-catalytic surface processes: Oxidation of toluene on CeO_2, Plasma Process Polym. 14 (2017) 1600114, https://doi.org/10.1002/ppap.201600114.
[47] X.i. Chen, J.-J. Li, X.i. Chen, S.-C. Cai, E.-Q. Yu, J. Chen, H. Jia, MOF-templated approach for hollow NiOx/Co_3O_4 catalysts: Enhanced light-driven thermocatalytic degradation of toluene, ACS Appl. Nano Mater. 1 (6) (2018) 2971–2981, https://doi.org/10.1021/acsanm.8b0058710.1021/acsanm.8b00587.s001.
[48] S. Huang, C. Zhang, H. He, Complete oxidation of o-xylene over Pd/Al_2O_3 catalyst at low temperature, Catal. Today. 139 (1-2) (2008) 15–23, https://doi.org/10.1016/j.cattod.2008.08.020.
[49] J.-H. Fu, Z. Zhong, D. Xie, Y.-J. Guo, D.-X. Kong, Z.-X. Zhao, Z.-X. Zhao, M. Li, SERS-Active MIL-100(Fe) Sensory Array for Ultrasensitive and Multiplex Detection of VOCs, Angew. Chem. Int. Ed. 59 (46) (2020) 20489–20498, https://doi.org/10.1002/anie.v59.4610.1002/anie.202002720.
[50] T. Ohno, Z. Miyamoto, K. Nishijima, H. Kanemitsu, F. Xueyuan, Sensitization of photocatalytic activity of S- or N-doped TiO_2 particles by adsorbing Fe^{3+} cations, Appl. Catal. A: Gen. 302 (2006) 62–68, https://doi.org/10.1016/j.apcata.2005.12.010.
[51] D. Wang, R. Huang, W. Liu, D. Sun, Z. Li, Fe-Based MOFs for Photocatalytic CO_2 reduction: role of coordination unsaturated sites and dual excitation pathways, ACS Catal. 4 (12) (2014) 4254–4260, https://doi.org/10.1021/cs501169t.